Coherent Fourier scatterometry nanoparticle detection enhanced by synthetic optical holography

Yin, Haoyang; Kolenov, Dmytro; Pereira, Silvania F.

DOI
10.1364/OL.463807

Publication date
2022

Document Version
Final published version

Published in
Optics Letters

Optics Letters

Coherent Fourier scatterometry nanoparticle detection enhanced by synthetic optical holography

Haoyang Yin, Dmytro Kolenov, and Silvania F. Pereira*

Optics Research Group, Imaging Physics Department, Faculty of Applied Sciences, Delft University of Technology, Lorentzweg 1, 2628 CJ Delft, The Netherlands
**Corresponding author: s.f.pereira@tudelft.nl*

Received 1 June 2022; revised 7 July 2022; accepted 8 July 2022; posted 8 July 2022; published 26 July 2022

We demonstrate that the sensitivity of nanoparticle detection on surfaces can be substantially improved by implementing synthetic optical holography (SOH) in coherent Fourier scatterometry (CFS), resulting in a phase-sensitive confocal differential detection technique that operates at very low power level ($P = 0.016$ mW). The improvement in sensitivity is due to two reasons: first, the boost in the signal at the detector due to the added reference beam; and second, the reduction of background noise caused by the electronics. With this new system, we are able to detect a 60-nm polystyrene latex (PSL) particle at a wavelength of 633 nm ($\sim\lambda/10$) on a silicon wafer with an improvement in the signal-to-noise ratio (SNR) of approximately 4 dB.

https://doi.org/10.1364/OL.463807

Introduction. As semiconductor devices shrink, the detection of contamination due to nanoparticles has become one of the major challenges in the semiconductor industry. These nanoparticles can cause major defects in semiconductor devices [1]. Therefore, the substrates and reticles need to be cleaned thoroughly and inspected before the fabrication process [2,3]. In addition to detection, simultaneous localization and classification of the nanoparticles without additional setups are often required. The detection system is ideally fast, sensitive, and should not damage the wafers with excessive illumination power.

The most used scattering-based particle detection system is the so-called dark-field technique. The dark-field technique is not limited by diffraction and background noise is avoided by selecting the angle of illumination that is different than the angle(s) of detection. However, if the particles are very small, the scattering signal is very low and, to achieve high signal-to-noise ratio (SNR), a high illumination power is often required [4]. This is particularly challenging in the detection of low scattering particles such as polystyrene latex (PSL) nanoparticles. Monodisperse polystyrene spheres are standard for metrology because of their traceable particle size. The large amount of energy needed to obtain a sufficient detected scattered signal can be a source of unwanted damage to the polymer coatings on a substrate [5].

In recent years, coherent Fourier scatterometry (CFS) has been introduced to tackle this problem. CFS is a bright-field scanning technique that is based on illuminating the sample with a focused coherent laser beam, and detecting the scattered and reflected field on a differential detector. CFS has been originally employed in grating metrology [6,7], but it also has been proven to be a noninvasive and sensitive technique for detecting nanoparticles on surfaces [8,9]. In practice, the CFS setup is similar to a confocal microscope where the sample is placed on a piezo scanning stage that moves in the lateral directions (perpendicular to the illumination beam) to perform a raster scan. A laser beam is focused on the sample with a high NA objective and the far field (Fourier plane) of the reflected light is imaged on a split detector, aligned in a way that the two halves of the detector are perpendicular to the scan direction. The difference between the two halves of the split detector gives a voltage value for the current scan position. If a particle-free surface is scanned, the far field of the laser beam is radially symmetric, thus the differential signal is zero for these positions. However, when a particle passes through the focused laser beam, the far field becomes asymmetric and position dependent. This asymmetry is detected as a differential signal that can be either positive or negative, depending on the position of the laser spot with respect to the center of the particle. The position of the particle can be determined by the differential signal and its size can be calibrated from the time span of the differential signal [8]. The performance of this technique is dictated by the signal-to-noise ratio (SNR) of the differential signal. It is well known that the scattering cross section decreases when the particle size shrinks [10]. Thus if one wants to detect very small nanoparticles (much smaller than the wavelength), it is important to eliminate or avoid all sources of noise that contribute to the detected signal. If one can achieve high SNR, then the speed of the scan can be increased or the illumination power can be reduced.

There are various techniques that have been implemented to improve the SNR of CFS, for instance, heterodyne detection [11], inner pupil blocking [8], and radially polarized light [12]. In this paper, we present a novel technique that has not been used before for the application of nanoparticle detection, which is the synthetic optical holography (SOH) phase-imaging technique [13–15]. The SOH scan setup is based on a confocal microscope operating in reflection in the sense that a laser beam is split in a

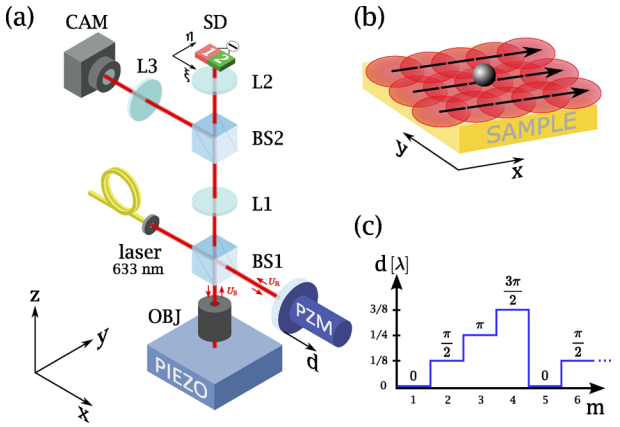

Fig. 1. (a) CFS setup with the implementation of SOH. OBJ, microscope objective (NA= 0.9); BS, (50/50) beam splitter; PZM, piezo-actuated mirror; L, lens; CAM, camera for localization and focusing; SD, split photo-detector. Coordinates (x, y, z) refer to the spatial position of the sample, d is the axial coordinate of the reference mirror, and (ξ, η) are spatial coordinates of the detector plane. (b) Raster scan scheme, where we typically only use the lines from left to right. (c) Position of the reference mirror for $N = 4$ mirror stepping movement. The resulting reference phase for each step is indicated on the graph.

beam splitter and directed to the sample arm where it is focused on the sample and a raster scan is performed. The difference between confocal microscopy and SOH is that in the latter, a reflective mirror is added at the open port of the beam splitter so that there is interference between the reflected beam from the sample and the reference beam before the detection takes place, similar to a Michelson interferometer. While the sample surface is being scanned, the reference mirror of the interferometer moves, creating a virtually tilted reference wave due to the phase change per scanned line. In this way, quantitative phase imaging in confocal microscopy can be achieved.

In this Letter, we integrate SOH phase imaging with the CFS setup. We refer to this new implementation as holographic coherent Fourier scatterometry (HCFS). Hereby, we demonstrate the performance enhancement of HCFS by detecting a PSL particle with a diameter of 60 nm at the wavelength of 633 nm ($\sim \lambda/10$) on a silicon wafer and compare the obtained SNR to that of conventional CFS under the same experimental conditions.

Implementation of SOH in CFS. The implementation of SOH in CFS is relatively straightforward, since we have to simply add a piezo-actuated mirror (PI P-841.1) at the open port of the beam splitter of our existing setup reported in [8]. The setup of HCFS is shown in Fig. 1(a). A collimated and linearly polarized He–Ne laser ($\lambda = 633$ nm) is coupled through a fiber and at its output, a fiber reflecting collimator based on a 90° parabolic mirror (Thorlabs RC08APC-P01) is placed to obtain a collimated beam of large diameter (≈8 mm). The beam splitter BS1 directs one beam into a microscope objective (NA = 0.9) that is focused on the sample of interest and another beam onto the piezo actuated reference mirror. The sample is placed on a piezo stage (PI P-629.2CD) that can be laterally scanned in a raster fashion [see Fig. 1(b)]. The reflected and scattered light from the sample arm U_S is collected by the objective and goes back into BS1, and is combined with the reflected reference beam U_R. The Fourier plane of the objective is de-magnified by a telescopic setup consisting of lenses L1, L2, L3, and beam splitter BS2, before being imaged simultaneously on a CCD camera and a split detector (ODD3W2 Bi-Cell Silicon Photodiode). The CCD camera is added only for alignment and localization of the area to be scanned. The split detector has effectively two pixels, and here the intensity voltage from the left pixel is subtracted from that of the right pixel, giving us a differential signal. At each scan position $\mathbf{r} = (x, y)$, the differential intensity of the interference pattern between the scattered beam $U_S(\mathbf{r})$ and the reference beam $U_R(\mathbf{r})$ is recorded.

While the sample is scanned, the reference mirror moves one step per scanned line creating a virtually tilted reference field $U_R(\mathbf{r}) = |U_R|e^{i\phi_R(\mathbf{r})} = |U_R|e^{i\mathbf{k}_\parallel \cdot \mathbf{r}}$. We define N as the number of lines or steps that the reference phase is changed by 2π. The position of the mirror d for line m is given by

$$d_m = \frac{\lambda}{2} \cdot \frac{\mathrm{mod}(m-1, N)}{N} \text{ for } m = 1, 2, 3 \cdots, \tag{1}$$

where λ is the wavelength of the laser beam and mod denotes the modulo division, e.g., $\mathrm{mod}(23, 5) = 3$. So, instead of stepping the mirror solely in the positive direction, we reset the mirror positions every N lines, because fields differing by 2π in phase can be regarded as identical. In Fig. 1(c), positions of the mirror are sketched for $N = 4$, where the reference phase repeats every four lines. The resulting virtual wave vector $\mathbf{k}_\parallel = (k_x, k_y)$ is given by

$$k_x = 0 \quad \text{and} \quad k_y = \frac{2\pi}{N\Delta y}, \tag{2}$$

where Δy is the line separation of the raster scan. The synthetic reference wave is analogous to a plane reference wave that is tilted in the y-direction.

The recorded differential hologram is described by

$$\begin{aligned} I(\mathbf{r}) &= I_1(\mathbf{r}) - I_2(\mathbf{r}) \\ &= \iint_{\mathrm{SD}_1} |U_R(\mathbf{r}) + U_S(\mathbf{r}, \xi_1, \eta_1)|^2 \, d\xi_1 d\eta_1 \\ &- \iint_{\mathrm{SD}_2} |U_R(\mathbf{r}) + U_S(\mathbf{r}, \xi_2, \eta_2)|^2 \, d\xi_2 d\eta_2 \,, \end{aligned} \tag{3}$$

where the signal for each position $\mathbf{r}$ equals the integrated intensity difference between the interference pattern on both sides of the detector. Subsequently, the expression can be reduced to three terms:

$$I(\mathbf{r}) = I_{\mathrm{diff,no\ mirror}}(\mathbf{r}) + |U_R|C^*(\mathbf{r})e^{i\phi_R(\mathbf{r})} + |U_R|C(\mathbf{r})e^{-i\phi_R(\mathbf{r})}. \tag{4}$$

Here, $I_{\mathrm{diff,no\ mirror}}$ is the conventional differential signal without the reference mirror and C is a complex term that is equal to the difference of the complex scattered field between both sides of the detector. They can be written as

$$\begin{aligned} I_{\mathrm{diff,no\ mirror}}(\mathbf{r}) &= \iint_{\mathrm{SD}_1} |U_S|^2 \, d\xi_1 d\eta_1 - \iint_{\mathrm{SD}_2} |U_S|^2 \, d\xi_2 d\eta_2, \\ C(\mathbf{r}) &= \iint_{\mathrm{SD}_1} U_S \, d\xi_1 d\eta_1 - \iint_{\mathrm{SD}_2} U_S \, d\xi_2 d\eta_2 \,. \end{aligned} \tag{5}$$

The reconstruction of the hologram is done in the same manner as the conventional off-axis digital holography [16,17], i.e., first we take the Fourier transform (FT) of Eq. (4):

$$\tilde{I}(\mathbf{q}) = \tilde{I}_{\mathrm{diff,no\ mirror}}(\mathbf{q}) + |U_R|\tilde{C}^*(\mathbf{q} - \mathbf{k}_\parallel) + |U_R|\tilde{C}(\mathbf{q} + \mathbf{k}_\parallel), \tag{6}$$

which contains the zero-order $\tilde{I}_{\mathrm{diff,no\ mirror}}$ (FT of the conventional CFS signal centered at DC), and two first orders centered at $\pm\mathbf{k}_\parallel$.

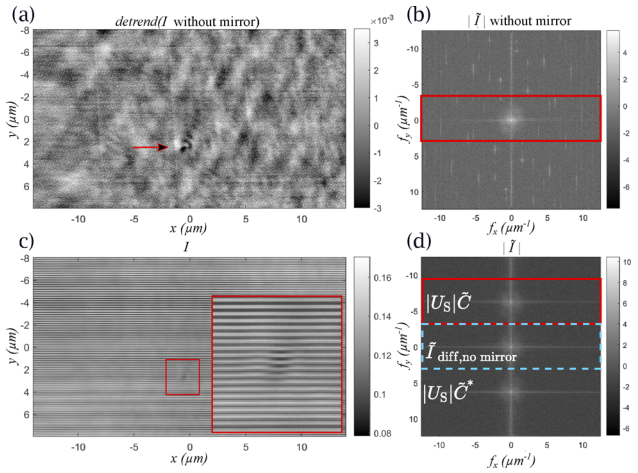

Fig. 2. (a) Conventional CFS measurement of a 60-nm PSL particle deposited on a Si wafer, where the signal due to the nanoparticle is indicated by an arrow. (b) Fourier transform of panel (a), logarithmic scale. The solid red window indicates where the filter is applied to reduce noise. (c) HCFS measurement of the scanned area with a zoom (bottom right) on the area where the nanoparticle is detected. (d) Fourier transform of panel (c), logarithmic scale. The solid red window indicates the first order, and the dashed blue window indicates the zero order. Image properties: 700 × 400 pixels; 28 μm × 16 μm; imaging time, 80 seconds.

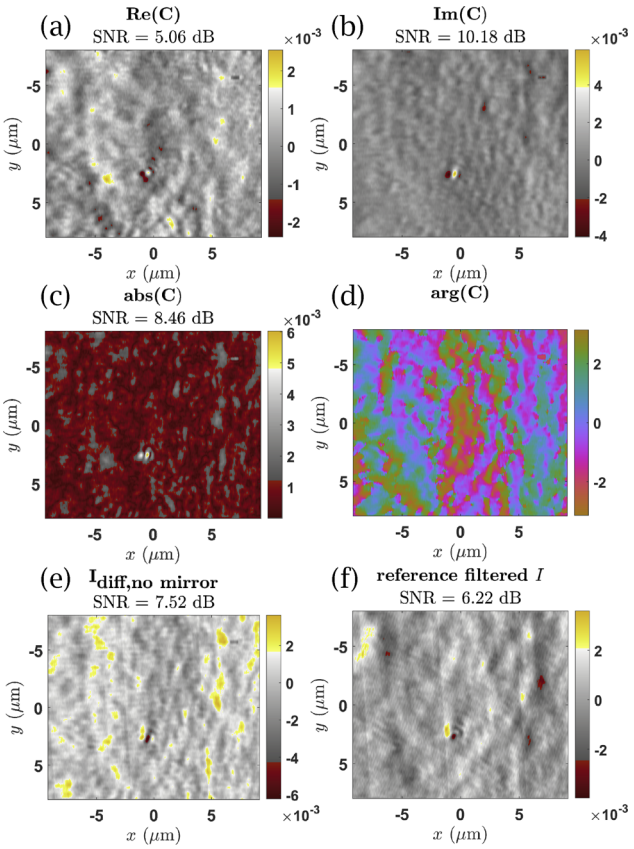

Fig. 3. (a) Real component, (b) imaginary component, (c) amplitude, and (d) argument of the first-order reconstruction $|U_R|C$. (e) Zero-order reconstruction $I_{\text{diff,no mirror}}$. (f) Filtered signal of conventional CFS with the same bandpass filter. For each plot, 4.8 μm of data are removed from both sides of x to eliminate artifacts at the edges, then the SNRs are computed and shown.

Second, we isolate the term $|U_R|\tilde{C}$ in Fourier space followed by shifting and inverse FT to retrieve information of the complex field differences C. Note that this conjugated term contains the constant reference field amplitude $|U_R|$, while the term $I_{\text{diff,no mirror}}$ does not depend on it. Since the silicon wafer only has a reflectivity of approximately 30% [18] at 633 nm, the reference field from the aluminum mirror will have a greater amplitude than the reflected field from the sample. This gives an interferometric amplification of the term $C(\mathbf{r})$, which can significantly improve the sensitivity for detecting particles.

We define the signal-to-noise ratio (SNR) as

$$\text{SNR}_{\text{dB}} = 10\log_{10}\left(\frac{P_S}{P_N}\right). \tag{7}$$

Here, P_S is the power of the signal part and P_N is the power of the noise part of the scan. For a measurement, we define the signal part that contains a particle with a circular mask, where data outside this mask are considered as noise.

Results. We demonstrate the application of HCFS by measuring a polystyrene latex (PSL) nanosphere with a diameter of 60 nm ($\sim \lambda/10$) using 0.016 mW of incident power on the Si wafer. We start by showing a measurement of the particle using the conventional CFS [Fig. 2(a), FT in Fig. 2(b)]. The location of the particle is indicated by the arrow. We can see in this case that the SNR of the signal from the nanoparticle is low (≈3 dB).

Next, using HCFS with $N = 4$ mirror stepping movement, i.e., at every four lines the reference phase changes by 2π, we recorded the hologram I [Fig. 2(c), FT in Fig. 2(d)]. The zoom on the bottom right of the figure shows a clear fringe pattern on the particle. We see also that the background also exhibits some fringe pattern, while in theory, it should be uniform and have value zero. The reason for this could be that there is slightly asymmetrical interference pattern at the split detector due to aberrations and beam non-uniformity, since we observe that the pattern changes each time the reference mirror moves. Nonetheless, these fringes do not affect the final result.

We follow the Fourier reconstruction procedure using a bandpass filter, which consists of a 2D cosine window superimposed with a high-pass filter in the f_x-direction. The size of the window is indicated in Fig. 2(d). The first- and zero-order reconstructions are shown in Figs. 3(a)–3(e) together with their SNRs. Also, the noise filtered map of the conventional CFS with the same filter is included as a reference [Fig. 3(f)]. We see both the real and imaginary parts [Figs. 3(a) and 3(b)] of the first order contain a signal that is similar to the conventional CFS signal in shape, where two peaks with opposite signs are located adjacent to each other. The same complex signal can also be represented with amplitude and phase. The amplitude [Fig. 3(c)] contains two symmetrical peaks, similar to the conventional CFS. However, the argument of C [Fig. 3(d)] does not help us distinguish the particle from the background, because the value is arbitrary in the background due to noise. Furthermore, the zero-order signal of HCFS [Fig. 3(e)] contains the same information as the conventional CFS.

Regarding the signal-to-noise ratios, with the imaginary part of the first-order signal [Fig. 3(b)], one achieves an SNR of approximately 10 dB, despite the size of the particle and the wavelength of our laser. Therefore, we expect that this setup is able to detect even smaller PSL particles at the current

power level. Compared to the reference, HCFS has a higher signal amplitude, and an SNR gain of 7 dB is achieved over the unfiltered signal or a gain of 4 dB over the filtered signal. While dealing with low SNR measurements, an SNR increase of 4 dB is quite meaningful, as it makes the particle much more distinguishable from the background.

Discussion. The main reason we are able to achieve a higher SNR is that the relatively strong reference field amplifies the first-order signal. Another reason is that the first-order signal avoids the low-frequency noise, such as $1/f$ noise of the electronic components (typically <200 Hz), electrical interference, and cross talk (50–60 Hz), similar to the heterodyne detection [11].

For the reconstruction of HCFS, we used a non-trivial bandpass filter. In this case, the filter consists of a 2D cosine window superimposed with a high-pass filter only in the f_x-direction. This is because we need to eliminate the vertical frequencies that distort the background of the reconstruction. This artifact comes mainly from aberrations, mirror instabilities, and background fluctuations, e.g., air turbulence and thermal expansion [13]. Also, we can justify cutting out these frequencies, because the expected particle signal (dipole-like) does not occupy this part of the Fourier spectrum. Furthermore, there are horizontal frequency components at each order, which we suspect that they are caused by the tilt of the sample. After reconstruction, this artifact results in big swings in amplitude near the left and right edges on the image. For now, we deal with it by cropping the edges of the image, meaning some loss of information. Thus, further optimization is needed for alignments, external vibrations, and precision of the piezo stages.

Conclusion. We demonstrated the use of synthetic optical holography (SOH) as a novel method to improve the sensitivity of coherent Fourier scatterometry (CFS) for particle detection. By adding a piezo-actuated reference mirror to the CFS setup, we can change the phase of the reference wave for every line of the raster scan, such that the 2D scan represents a digital off-axis hologram. The hologram from this combined technique (HCFS) contains the conventional CFS differential signal as the zero order, and two first-order signals equal the complex far-field difference scaled by the reference field amplitude. For the detection of a polystyrene latex (PSL) particle with a diameter of 60 nm ($\sim \lambda/10$) on a silicon wafer, we achieved an SNR gain of approximately 4 dB compared to the conventional CFS after noise filtering, mainly due to the interferometric signal boost. However, HCFS is more prone to mechanical instabilities and alignment tolerances compared to its predecessor.

Beyond the detection of particles on wafers, HCFS could also be employed when the contrast between the nanoparticles and substrate is low, such as PSL particles on glass or pellicle. Due to the phase sensitive nature, HCFS could be much more sensitive than conventional CFS in these use cases. Furthermore, due to the modulation property, HCFS is also suitable for low-power applications, such as cellular imaging [19,20].

Funding. Nederlandse Organisatie voor Wetenschappelijk Onderzoek (P17-24 project 2).

Acknowledgments. We would like to thank Prof. Martin Hofmann from the Ruhr University Bochum, Germany and members of his group for introducing us to SOH and for fruitful discussions during visits between the two groups. We also acknowledge Roland Horsten and Thim Zuidwijk for their technical support.

Disclosures. The authors declare no conflicts of interest.

Data availability. Data underlying the results presented in this paper are not publicly available at this time but may be obtained from the authors upon reasonable request.

REFERENCES

1. A. Chen, V. Huang, S. Chen, C. Tsai, K. Wu, H. Zhang, K. Sun, J. Saito, H. Chen, D. Hu, L. Ming, W. Shen, and U. Mahajan, Lithogr. Asia 2008 **7140**, 71400W (2008).
2. L. Scaccabarozzi, N. Lammers, R. Moors, and V. Banine, "Cleaning and inspection of EUV reticles: specifications and prospects," https://api.semanticscholar.org/CorpusID:173985123.
3. M. van de Kerkhof, T. van Empel, M. Lercel, C. Smeets, F. van de Wetering, A. Nikipelov, C. Cloin, A. Yakunin, and V. Banine, Extrem. Ultrav. (EUV) Lithogr. X **10957**, 27 (2019).
4. J. van der Donck, R. Snel, J. Stortelder, A. Abutan, S. Oostrom, S. van Reek, B. van der Zwan, and P. van der Walle, Extrem. Ultrav. (EUV) Lithogr. X **7969**, 79691S (2011).
5. J. Pospıšil and S. Nešpurek, Prog. Polym. Sci. **25**, 1261 (2000).
6. N. Kumar, P. Petrik, G. Ramanandan, O. El Gawhary, S. Roy, S. Pereira, W. Coene, and H. Urbach, Opt. Express **22**, 24678 (2014).
7. N. Kumar, L. Cisotto, S. Roy, G. Ramanandan, S. Pereira, and H. Urbach, Appl. Opt. **55**, 4408 (2016).
8. S. Roy, M. Bouwens, L. Wei, S. Pereira, H. Urbach, and P. Van Der Walle, Rev. Sci. Instrum. **86**, 123111 (2015).
9. D. Kolenov, I. Zadeh, R. Horsten, and S. Pereira, Opt. Express **29**, 16487 (2021).
10. A. Cox, A. DeWeerd, and J. Linden, Am. J. Phys. **70**, 620 (2002).
11. D. Kolenov, R. Horsten, and S. Pereira, Opt. Meas. Syst. for Ind. Insp. XI **11056**, 45 (2019).
12. S. Roy, K. Ushakova, Q. Van den Berg, S. Pereira, and H. Urbach, Phys. Rev. Lett. **114**, 103903 (2015).
13. M. Schnell, M. Perez-Roldan, P. Carney, and R. Hillenbrand, Opt. Express **22**, 15267 (2014).
14. M. Schnell, P. Carney, and R. Hillenbrand, Nat. Commun. **5**, 1 (2014).
15. L. Schnitzler, K. Neutsch, F. Schellenberg, M. R. Hofmann, and N. C. Gerhardt, Appl. Opt. **60**, A8 (2021).
16. T. Poon and J. Liu, *Introduction to Modern Digital Holography: with MATLAB* (Cambridge University Press, 2014).
17. E. Cuche, P. Marquet, and C. Depeursinge, Appl. Opt. **39**, 4070 (2000).
18. G. Moona, P. Kapruwan, R. Sharma, and V. Ojha, Proc. Natl. Acad. Sci., India, Sect. A Phys. Sci. **88**, 617 (2018).
19. V. Backman, V. Gopal, M. Kalashnikov, K. Badizadegan, R. Gurjar, A. Wax, I. Georgakoudi, M. Mueller, C. Boone, R. Dasari, and M. Feld, IEEE J. Sel. Top. Quantum Electron. **7**, 887 (2001).
20. O. Marina, C. Sanders, and J. Mourant, Biomed. Opt. Express **3**, 296 (2012).